

Cascade hot carriers via broad-band resonant tunneling

Kamal Kumar Paul¹, Ashok Mondal^{1,2}, Jae Woo Kim^{1,2}, Ji-Hee Kim^{1,2,*}, and Young Hee Lee^{1,2,3,*}

¹Center for Integrated Nanostructure Physics, Institute for Basic Science, Sungkyunkwan University, Suwon, Republic of Korea

²Department of Energy Science, Sungkyunkwan University, Suwon 16419, Republic of Korea

³Department of Physics, Sungkyunkwan University, Suwon 16419, Republic of Korea

*kimj@skku.edu, leeyoung@skku.edu

Extraction of hot carriers (HCs) over the band-edge is a key to harvest solar energy beyond Shockley-Queisser limit¹. Graphene is known as a HC-layered material due to phonon bottleneck effect near Dirac point, but limited by low photocarrier density². Graphene/transition metal dichalcogenide (TMD) heterostructures circumvent this issue by ultrafast carrier transfer from TMD to graphene^{2,3}. Nevertheless, efficient extraction of photocurrent by means of HCs together with carrier multiplication (CM) is still missing. Here, we introduce an ultrathin broadband resonant tunneling (BRT) barrier, TiO_x to efficiently extract photocurrent with simultaneous CM and HC measurements in MoS₂/graphene/TiO_x heterostructure. The BRT layer gives rise to boosting open circuit voltage which is linearly proportional to incident photon energy. Meanwhile, short circuit current rises rapidly over $2E_g$ with obvious CM feature. This was explained by defining the joint density of states between graphene and TiO_x layer over positive and negative voltage. The broadband resonant tunneling states inherently constructed from oxidation states varying from Ti³⁺ to Ti⁴⁺ allow the ultrafast HCs to efficiently transfer from graphene to TiO_x layer. We find that the number of available tunneling states is directly proportional to short circuit current, which is well corroborated with TiO_x and MoS₂ thickness variance. We obtained an optimum thickness of BRT layer of ~2.8 nm, yielding cascade open circuit voltage as high as ~0.7 V, two orders of magnitude higher than that without BRT layer to reach a record efficiency of 5.3% with improved fill factor owing to synergistic HC and CM conversion under 1-SUN with long-term stability.

Manipulation of relaxation and extraction of the photo-excited carriers is one of the key factors for efficient hot carrier-driven photocatalytic, optoelectronic and photovoltaic applications^{1,4,5}. The photo-generated carriers beyond the band-edge, often referred to as hot carriers (HCs), lead to heat dissipation through carrier-phonon scattering and finally arrive at the band-edge to contribute to photocurrent. This major intrinsic energy loss limits a maximum theoretical power conversion efficiency (PCE) of ~34% in a conventional single-junction solar cell under 1-SUN illumination⁶. HC-based solar cell essentially utilizes the excess energy of HCs to generate additional free carriers

or free energy. This leads to enhanced short circuit current (J_{SC}) in carrier multiplication (CM) solar cell with a maximum PCE of $\sim 46\%$ ^{7,8} and improved open circuit voltage (V_{OC}) in HC solar cell with a maximum PCE of $\sim 67\%$ beyond Shockley-Queisser limit^{9,10}. Efficient extraction of HCs to proliferate PCE is prerequisite to retain prolonged relaxation and more importantly, to extract HCs to the contact, often known as energy selective contact¹¹.

Numerous bulk materials including GaAs¹² and InN¹³ have been proposed as a HC absorber with high carrier mobility and phononic bandgap. Extraction of HCs has been inefficient so far, however, primarily due to poorly implemented phonon bottleneck effect and energy selective contact^{1,14}. Low-dimensional confined systems such as quantum dots (QDs) and van der Waals (vdWs) layered transition metal dichalcogenides (TMDs) predominantly involve strong Coulomb interaction and thus improve CM^{8,15–20}. Nevertheless, QD structures via CM have been reported with inefficient carrier extraction due to the charge localization, low carrier mobility and diffusion length^{21–24}. In particular, one unique feature in graphene (Gr) is linear band dispersion, where the carrier density vanishes near the Dirac point to persist in prolonged lifetime, resulting in strong phonon bottleneck effect at low energy of < 200 meV near the Dirac point, i.e., hence HC effect^{5,25–28}. While evidence of HCs has been demonstrated in Gr with clear phonon bottleneck effect, V_{OC} is still limited to a few mV and furthermore, Gr possesses considerably low optical absorbance ($\sim 2.3\%$ / monolayer) compared to that of vdW TMD materials (MoS₂, MoSe₂, WS₂, etc.) which exhibits relatively high absorbance ($\sim 5\text{-}10\%$ / monolayer)^{2,5}. An atomically thin MoS₂/Gr heterostructure demonstrates efficient nondissipative interfacial HC transfer from MoS₂ to Gr using ultrafast transient absorption spectroscopy, thereby increasing the photogenerated carrier population. Despite the promising conjectures^{2,3,29}, the design of Gr-based TMD architecture to improve amenable solar cell efficiency involving HCs and CM is still challenging¹.

In this article, we propose an ultrathin TiO_x layer for broadband resonant tunneling to cascade open circuit voltage for HCs in MoS₂/Gr heterostructure device. The Gr layer is sandwiched between multilayer MoS₂ and TiO_x layer. We introduce the joint density of states between Gr and TiO_x layer to explain the broadband tunneling states in TiO_x layer which is directly correlated to V_{OC} in HC to further boost J_{SC} in CM. Our report demonstrates the first proof-of-concept of HC solar cell based on vdWs MoS₂/Gr heterostructure boosted by the ultrafast transfer of multiplied HCs from MoS₂ to Gr² and predominant phonon bottleneck effect in Gr, followed by the broadband resonant tunneling (BRT) through ultrathin BRT layer (TiO_x).

Direct photocurrent measurement for carrier multiplication

Figure 1a shows the schematic of CM in MoS₂ with the optical excitation above $2E_g$ (process 1) and inverse Auger recombination (process 2). The vdW TMD materials are known to manifest low CM threshold energy of nearly two times the bandgap and ideal ($\sim 99\%$) CM conversion efficiency due to strong Coulomb interaction and quantum confinement effect using transient absorption spectroscopy⁸. Photoexcited carriers generate abundant HCs in MoS₂ and are ultrafast-transferred

to Gr to become hotter due to phonon bottleneck effect and finally extract carriers to Ti electrode (Fig. 1b)². Despite the presence of rich HCs in Gr, they become cold due to similar work function between Gr and Ti, leaving negligible V_{OC} ³⁰. Therefore, robust design of Gr-based TMD architecture is prerequisite. The reported vertical/ lateral structures have been mostly utilized by the Schottky barrier/ asymmetric electrodes and/or doping (chemically/ electrostatically) without considering the HCs (see Supplementary Table 1). We propose ultrathin TiO_x layer as a broadband resonant tunneling barrier (Fig. 1c). TiO_x layer is deposited onto Gr to efficiently extract multiplied HCs to elevate V_{OC} as well as J_{SC} . The TiO_x layer plays a role as tunneling from cascade HC energies resonant by the presence of wide range of oxidation states, i.e., broadband resonant tunneling. Formation of the ultrathin TiO_x layer is the key to create the broadband tunneling states ranging from Ti^{3+} to Ti^{4+} oxidation states so that HCs can be extracted with high V_{OC} . Furthermore, optimum thickness for tunneling is required to maximize the current density. This is conceptually distinguished from energy selective contact in bulk.^{11,31}

Figure 1d shows current-voltage characteristics of $MoS_2/Gr/Ti$ cell with various laser energies at a fixed absorbed photon density (Supplementary Fig. 1). V_{OC} is negligibly small with ~ 10 mV for excitation laser energies up to 3.31 eV, which is still limited for HC extraction. Meanwhile, the photocurrent density is linearly proportional to the absorbed photon density up to $\sim 1.4 \times 10^{15} \text{ cm}^{-2} \text{ s}^{-1}$ with various excited energies where the absorbed photon density is multiplied by absorbance of the device (1.53 eV – 3.31 eV (Fig. 1e and see Extended Data Fig. 1 with the corresponding absorbance values in Supplementary Table 2). This excludes possibility of many-body interaction³². The linear slope is still retained with abrupt slope change beyond 2.54 eV ($2E_g$). The quantum yield can be defined by the slope at a given excitation photon energy, $QY = S_E/S_{2E_g}$ similar to previous report³². Figure 1f shows a clear CM feature in MoS_2 from MoS_2/Gr cell from photocurrent measurement. The quantum yield abruptly rises above $2E_g$ and approaches to as high as 200% at $3E_g$. Meanwhile, it is remarkable to observe an escalated V_{OC} of ~ 0.7 V by two orders of magnitude in $MoS_2/Gr/TiO_x$ cell (Fig. 1g). Furthermore, J_{SC} is enhanced to 5.7 mA cm^{-2} by 14 times with enhanced quantum efficiency (Fig. 1h, i), similar to that of MoS_2/Gr cell.

Cascade hot carriers to elevate V_{OC} in $MoS_2/Gr/TiO_x$ heterostructure

Despite the similar CM conversion efficiency regardless of TiO_x inclusion in the cell, V_{OC} is elevated by two orders of magnitude by depositing TiO_x layer on Gr by atomic layer deposition, where the MoS_2/Gr heterojunction is constructed by vdWs assembly of individual material on hBN substrate (Fig. 2a,b) (See Methods and Supplementary Fig. 2). To understand the underlying mechanism, we investigated the photocells with various photon densities and energies as well as TiO_x layer thicknesses. Figure 2c presents the representative I-V curves by illuminating various photon densities at different photon energies (3.31 eV, 1.94 eV and 1.53 eV) for a given TiO_x thickness of 2.8 nm (See Supplementary Fig. 3 for other energies). Both V_{OC} and J_{SC} are remarkably enhanced at higher incident energy of 3.31 eV ($> 2E_g$) compared to low energy of 1.94 eV or 1.53 eV ($< 2E_g$). Figure 2d shows V_{OC} with absorbed photon density for given photon energy.

V_{OC} rises sharply at low fluence and saturates at higher fluence. Unlike conventional solar cell, owning the V_{OC} insensitive to incident energy, a HC solar cell in principle possesses dynamic V_{OC} varying with excitation energy (Fig. 2d). Unlike low V_{OC} of ~ 10 mV in MoS₂/Gr/Ti cell, the cascade V_{OC} as high as 0.7 V is clearly manifested in MoS₂/Gr/TiO_x/Ti cell. V_{OC} is linearly proportional to incident energy below $2E_g$ and saturates at higher energy (Fig. 2e) with no distinct threshold energy of $2E_g$.

Such a systematic V_{OC} enhancement ensures the efficient extraction of HCs in the presence of TiO_x layer. Gr/TiO_x/Ti cell without MoS₂ still exhibits comparatively amenable photovoltaic characteristics due to HC extraction with medium V_{OC} , indicating importance of the TiO_x layer (See Extended Data Fig. 2). This is confirmed again by negligibly low V_{OC} in MoS₂/Gr/Ti cell without TiO_x layer caused by the well-known photothermal effect, similar to previous report in the Gr-metal interfaces⁵. The J_{SC} increases linearly with incident energy below $2E_g$ and rises rapidly at $> 2E_g$ in MoS₂/Gr/TiO_x cell (Fig. 2f), indicating the CM effect similar to Figure 1i. Similar CM effect was observed in MoS₂/Gr/Ti cell without TiO_x layer in Fig. 1f. Such a CM feature is not clearly visible in the absence of MoS₂ in Gr/TiO_x cell, still retaining amenable J_{SC} , where the reasonable V_{OC} in TiO_x layer still contributes to J_{SC} . MoS₂ generates additional carriers via CM but fails to extract carriers to Ti layer (low work function difference) in MoS₂/Gr/Ti cell. In Gr/TiO_x cell, both CM and HCs are provoked in Gr and efficiently extracted through TiO_x BRT barrier to reveal reasonable J_{SC} . In ideal MoS₂/Gr/TiO_x cell, both CM from MoS₂ and Gr, and efficient HC extraction though TiO_x layer enhances both J_{SC} and V_{OC} .

Optimum thicknesses of TiO_x and MoS₂ layer

Figure 3 shows the photovoltaic characteristics on the BRT layer and MoS₂ film thicknesses for a given incident energy of 3.31 eV. At ~ 1 nm thin TiO_x layer, the leakage current is dominant from negative voltage and hence V_{OC} remains small (Fig. 3a). As the TiO_x layer becomes thicker, the leakage current seemingly becomes smaller. Both V_{OC} and J_{SC} are enhanced particularly at 2.8 nm and are degraded at thicker layers (see Supplementary Fig. 4). V_{OC} increases as a function of photon flux to saturate at higher photon density (Fig. 3b) owing to band filling effect^{32,33}, which reaches the maximum at a TiO_x layer of 2.8 nm. Similarly, the J_{SC} is maximum at a TiO_x layer of 2.8 nm (Fig. 3c). The maximum V_{OC} and J_{SC} are clearly observed at an optimum TiO_x layer thickness of 2.8 nm (Fig. 3d,e). At ultrathin TiO_x layer i.e., 1 nm, the leakage is dominant and V_{OC} is not matured yet, limiting J_{SC} . At an optimum TiO_x layer of 2.8 nm, the leakage current is minimized, resulting in maximum J_{SC} . At a thick TiO_x layer over 2.8 nm, the J_{SC} is degraded. Similarly, V_{OC} rises with increasing TiO_x layer. At thick TiO_x layer, the surface states are relatively reduced with remaining bulk states to consequently reduce V_{OC} .

Figure 3f presents the I-V characteristics with various MoS₂ film thicknesses (1.4 – 20 nm) at a fixed BRT layer thickness of 2.8 nm with 3.31 eV (details shown in Supplementary Fig. 5). We plot V_{OC} (Fig. 3g) and J_{SC} (Fig. 3h) with absorbed photon density, revealing the systematic uptakes with the MoS₂ film thicknesses. J_{SC} is linearly proportional at thin MoS₂ layer and saturates at

thick MoS₂ layer (Fig. 3i). This can be fitted to $J = J_0 - J^{max} e^{-x/\lambda}$, where $J_0 = J_{Gr} + J^{max}$, J_{Gr} is the maximum current density value for Gr/TiO_x cell without MoS₂, and J^{max} is the current density in the presence of MoS₂. The characteristic diffusion length of carrier, λ is estimated as ~6.5 nm. Thick layer over λ , i.e., ~30 nm reaches maximum J_{SC} due to diffusion limit. Thicker MoS₂ absorbs more excited carriers due to enhanced absorbance to further proliferate more excited carriers via CM. These are further transferred to Gr layer to become hotter to contribute higher V_{OC} owing to band filling effect (Fig. 3j).

Manifestation of resonant tunneling states in TiO_x layer

So far, we observed the cascade V_{OC} and J_{SC} in terms of CM and HCs in MoS₂/Gr/TiO_x heterostructure by introducing the BRT barrier with an ultrathin TiO_x layer. To understand microscopic origin of BRT barrier, we analyzed oxidation states of the TiO_x layer using XPS and the joint density of states (dI/dV) of the heterostructure cell. Figure 4a represents the schematic of broadband resonant tunneling states inherently constructed from oxidation states in TiO_x layer varying with Ti^{3+ δ} . Ultrathin TiO_x layer with various oxidation states (Ti^{3+ δ} , $\delta = 0$ to 1) forms a broadband tunneling states and thus enables a cascade tunneling resonant with energy of the multiplied hot electrons in Gr, while completely blocking the holes (Fig. 4a). Existence of the different oxidation states in BRT barrier is confirmed by O1s (Fig. 4b) and Ti2p (Fig. 4c) core-level XPS spectra, identifying Ti³⁺ and Ti⁴⁺ oxidation states^{34,35}. Both surface states and bulk states may vary under different environmental conditions including structural deformation in TiO_x lattice, hence defined as Ti^{3+ δ} , $\delta = 0$ to 1.

Figure 4d represents the joint density of states dI/dV between Gr and TiO_x layer with various TiO_x layer thicknesses. Each curve is color-filled up to 1st peak minimum, which is equivalent to V_{OC}. At thick TiO_x layer of 6 nm, the bulk states prevail with relatively low V_{OC}. At lower TiO_x layer of 5 nm, the surface states start to emerge and hence increase V_{OC}, while the bulk states shrink. The surface states become maximum at TiO_x layer of 2.8 nm, eventually maximizing V_{OC}, while still retaining amenable bulk states. The number of available tunneling states can be obtained by integrating dI/dV over the positive voltage,

$$N_{TS} = \int_{V=0}^{V_{OC}} (dI/dV)_V dV. \quad (1)$$

N_{TS} is maximum at TiO_x layer of 2.8 nm (Fig. 4e), similar to V_{OC} and J_{SC}. Such a trend in TiO_x layer thickness is different from that in MoS₂ channel thickness. N_{TS} seemingly rises with increasing MoS₂ layer thickness (Fig. 4f) due to multiplied carriers in MoS₂ layer to transfer to Gr, eventually contributing to J_{SC} through BRT barrier. The N_{TS} in Figure 4g is congruent with J_{SC} behavior observed in Figure 3i.

The number of leakage states, N_{LS} , can be similarly defined by integration of dI/dV over the negative voltage,

$$N_{LS} = \int_{V=0}^{-V} (dI/dV)_V dV. \quad (2)$$

Figure 4h summarizes N_{LS} in terms of MoS₂ thickness (See **Extended Data Fig. 3a**). The leakage current is provoked by the presence of traps at MoS₂/Gr interface during ultrafast photoexcited carrier transfer from MoS₂ to Gr layer. At 1.4 nm thin MoS₂ layer, N_{LS} prevails by the ample surface states of MoS₂ layer and eventually saturates by minimizing the trap density at thicker MoS₂ layer. Such a reduction of N_{LS} with increasing MoS₂ layer thickness is well understood by inversely proportional J_{SC} . Similarly, N_{LS} prevails at 1 nm thin TiO_x layer due to the dominant back scattering of premature V_{OC} (**Extended Data Fig. 3b,c**). The N_{LS} rapidly drops at 2.8 nm thin TiO_x layer due to ample tunneling states of mature V_{OC} . This further saturates at thicker TiO_x layers in accordance with the degraded V_{OC} or J_{SC} . Analysis of N_{LS} is complementary to understand the photovoltaic performance together with V_{OC} and J_{SC} .

Solar cell performance of various heterostructures under 1-SUN illumination

Figure 5a depicts photocurrent density vs. voltage of different cells MoS₂/Gr/Ti, Gr/TiO_x/Ti, MoS₂/Gr/TiO_x/Ti and MoS₂/Gr/TiO_x under 1-SUN illumination (AM 1.5 G). We observe remarkable cell performance for MoS₂/Gr/TiO_x/Ti with improved V_{OC} and J_{SC} compared to MoS₂/Gr/Ti or Gr/TiO_x/Ti cell. Such superb photovoltaic performance in MoS₂/Gr/TiO_x/Ti (**Fig. 5b**) is well explained by the significantly reduced number of leakage states at negative voltage (**Extended Data Fig. 4a**). This again reassures that such an analysis of N_{TS} (**Extended Data Fig. 4b**) at positive voltage and N_{LS} at negative voltage is inherent to explain origin of V_{OC} and J_{SC} under 1-SUN illumination.

The photovoltaic performance is enhanced further in MoS₂/Gr/TiO_x cell under equivalent 1-SUN illumination (considering the transmission loss due to the top Ti electrode). The fill factor (FF) reaches as large as 63.4% in MoS₂/Gr/TiO_x cell (**Fig. 5c**), similar to other materials such as perovskites^{36,37} or Si/perovskite tandem solar cells³⁸, over two times larger than in MoS₂/Gr cell due to inherent construction of the BRT barrier with optimized TiO_x layer thickness. The HC-dominant Gr/TiO_x/Ti cell outperforms the CM-dominant MoS₂/Gr/Ti cell by two orders of magnitude higher PCE (**Fig. 5c**). Surprisingly, we observe the improved PCE of 5.3% in MoS₂/Gr/TiO_x cell via synergistic effects of HCs and CM. Efficient HC extraction with synergistic CM in TMD materials by introducing ultrathin BRT layer has not been observed previously to date. The extracted electrical power density (P_{el} = photocurrent density × voltage) versus voltage is shown for different cells (**Fig. 5c, inset**). The maximum electrical output power density ($P_{el,m}$) for MoS₂/Gr/TiO_x/Ti cell is 3.5 mW cm⁻² at 0.52 V, which is further enhanced to 5.3 mW cm⁻² at 0.54 V for MoS₂/Gr/TiO_x cell with three orders of magnitude higher than MoS₂/Gr/Ti cell ($P_{el,m}$ = 0.001 mW cm⁻² at 0.006 V). **Figure 5d** further demonstrates the long-term operational stability of MoS₂/Gr/TiO_x cell under regular laboratory environment (see **Methods**), by revealing the persistent PCE with negligible fall even after 120 days, which establishes the stability of our HC-solar cell in TMD materials.

Conclusion

We have introduced an ultrathin broadband resonant tunneling (BRT) barrier, TiO_x to boost open circuit voltage and further improve photocurrent extraction from simultaneous measurements of CM and HC in $\text{MoS}_2/\text{Gr}/\text{TiO}_x$ heterostructure. Ultrafast-transferred multicarriers from MoS_2 enrich HCs in Gr due to phonon bottleneck effect. The cascade HC energies in Gr resonant with the broadband oxidation states in ultrathin TiO_x layer ($\text{Ti}^{3+\delta}$, $\delta = 0$ to 1) are harvested efficiently via broadband resonant tunneling, elevating both V_{OC} and J_{SC} . We were able to demonstrate the presence of broadband resonant tunneling states between Gr and TiO_x layer by integrating joint density of states of dI/dV . The number of available tunneling states is directly proportional to short circuit current, which is well corroborated with TiO_x and MoS_2 thickness variance. Although $\text{MoS}_2/\text{Gr}/\text{TiO}_x$ cell provides the PCE of $\sim 5.3\%$ with synergistic contribution of HCs and CM, this is just an infant stage to develop. There is plenty of room to revolutionize PCE improvement in TMD materials. Both optical and electronic designs need to be improved. The optical absorption of our vdWs heterojunction is only $\sim 50\%$, which may be improved by replacing the TMD material or different device architecture³⁹. The 5 nm thin top Ti contact layer is inevitably oxidized from its surface, thereby increasing the contact resistance. Moreover, the absorbed optical power in TMD/Gr heterostructure is weakened due to undesirable absorption in top Ti electrode, which could be rectified with an inverted cell architecture. Photovoltaic performance could be tuned further with suitable substitution of the BRT layer, or by engineering the BRT layer i.e., broadening the oxidation states, by increasing the available tunneling states and V_{OC} . Alternatively, different BRT barrier materials could be explored for optimizing PCE. Our proposal to analyzing resonant tunneling states using dI/dV and its integration at positive voltage and leakage current at negative voltage will provide deep insight to develop next-generation solar cells for other materials including perovskites and heterostructures.

Methods

Device fabrication

MoS_2 with various thicknesses ($\sim 1.4 - 20$ nm), Gr (~ 2 nm), and hBN ($\sim 15 - 30$ nm) were mechanically exfoliated from commercially available high-quality bulk crystals (2D Semiconductors, USA). To fabricate hBN/ MoS_2 /Gr vdWs heterostructures, the selected flakes were picked up and dry released on the Si/SiO₂ substrate by using PDMS/poly-propylene carbonate (PPC) stamp and a customized micro-manipulator. This technique excludes any interfacial contamination⁴⁰. To achieve the desired geometry, the vertical stacks were shaped by the standard electron-beam (e-beam) lithography with 950 PMMA A4 e-beam resist, and sequentially etched by O₂ (for Gr) as well as SF₆ (for hBN, MoS_2) plasma using reactive ion etching (RIE). The bottom contact on Gr were defined by e-beam lithography, following the metal electrode Cr/Au (5/40 nm) deposition using the thermal evaporator. The ultrathin BRT layer with various thicknesses (TiO_x : 1 – 6 nm) was then deposited on the heterojunction by using atomic layer deposition (ALD)⁴¹. Finally, one window was constructed precisely on the MoS_2/Gr

heterojunction for the top electrode by using e-beam lithography, followed by the deposition of thin Ti (5 nm) using ultra-high vacuum sputter ($\sim 10^{-7}$ torr) system.

Characterization

The photophysical properties of the individual material as well as the vertical heterostructure were investigated by atomic force microscopy (Seiko AFM 5000 II) and optical spectroscopy (Raman) using NT-MDT with 532 nm laser excitation. X-ray photoelectron spectroscopy (K-Alpha, THERMO FISHER) was employed to identify the various oxidation states of TiO_x layer. For absorption (A) measurements, reflection (R) and transmission (T) of the vdWs vertical stacks on transparent quartz substrate (transmission $\sim 95\%$) were measured. Transmission spectra were recorded on the heterojunction considering the bare quartz substrate as a reference. The reflection spectra on the sample were measured after the calibration with a silver mirror (PF10-03-P01, Thorlabs) for the absolute reflection spectrum. Finally, the following equation was used for the absorption calculation: $A(\lambda) = 1 - R(\lambda) - T(\lambda)$.

I-V measurements with lasers. Photocurrent measurements of various vertical cells ($\text{Gr}/\text{TiO}_x/\text{Ti}$, $\text{MoS}_2/\text{Gr}/\text{Ti}$ and $\text{MoS}_2/\text{Gr}/\text{TiO}_x/\text{Ti}$) were performed at the vacuum probe station ($\sim 10^{-6}$ torr) using Keithley 4200A. External laser linings with various energies (diode lasers; 1.53 – 3.31 eV) were integrated with the vacuum probe station, and precisely incident on the sample through the optical window.

1-SUN I-V measurements. To determine the PCE of the vertical cells under AM 1.5 G, I-V measurements were performed using a solar simulator (Oriel Sol3A, Newport) connected with a Keithley 2400 source meter. The lamp intensity was calibrated with a Si reference cell (Newport, Oriel 91150 V) precisely placed at the sample position. I-V curves were recorded in a normal lab environment (temperature: 22 °C; humidity: 35%). During the measurement, temperature of the sample was maintained via convection cooling with an electric fan. Photocurrent density as well as the PCE extracted from the continuous maximum power point tracking demonstrates the long-term operational stability of the cell under ambient conditions. I-V measurements were performed continuously for 3 hrs in each day and repeated for several times up to 120 days. In all I-V measurements, the voltage was applied to the Gr bottom contact, while the Ti top contact was grounded.

References

1. Paul, K. K., Kim, J.-H. & Lee, Y. H. Hot carrier photovoltaics in van der Waals heterostructures. *Nat. Rev. Phys.* **3**, 178–192 (2021).
2. Tran, M. D. *et al.* Decelerated Hot Carrier Cooling in Graphene via Nondissipative Carrier Injection from MoS₂. *ACS Nano* **14**, 13905–13912 (2020).
3. Wang, L. *et al.* Slow cooling and efficient extraction of C-exciton hot carriers in MoS₂ monolayer. *Nat. Commun.* **8**, 13906 (2017).
4. Yan, Y. *et al.* Multiple exciton generation for photoelectrochemical hydrogen evolution reactions with quantum yields exceeding 100%. *Nat. Energy* **2**, 1–7 (2017).
5. Gabor, N. M. *et al.* Hot Carrier–Assisted Intrinsic Photoresponse in Graphene. *Science* **334**, 648–652 (2011).
6. Shockley, W. & Queisser, H. J. Detailed Balance Limit of Efficiency of p-n Junction Solar Cells. *J. Appl. Phys.* **32**, 510–519 (1961).
7. Beard, M. C., Luther, J. M., Semonin, O. E. & Nozik, A. J. Third Generation Photovoltaics based on Multiple Exciton Generation in Quantum Confined Semiconductors. *Acc. Chem. Res.* **46**, 1252–1260 (2013).
8. Kim, J.-H. *et al.* Carrier multiplication in van der Waals layered transition metal dichalcogenides. *Nat. Commun.* **10**, 5488 (2019).
9. Nozik, A. J. Utilizing hot electrons. *Nat. Energy* **3**, 170–171 (2018).
10. Conibeer, G. Third-generation photovoltaics. *Mater. Today* **10**, 42–50 (2007).
11. Conibeer, G. J. *et al.* Selective energy contacts for hot carrier solar cells. *Thin Solid Films* **516**, 6968–6973 (2008).
12. Yang, Y. *et al.* Observation of a hot-phonon bottleneck in lead-iodide perovskites. *Nat. Photonics* **10**, 53–59 (2016).
13. Wen, Y.-C., Chen, C.-Y., Shen, C.-H., Gwo, S. & Sun, C.-K. Ultrafast carrier thermalization in InN. *Appl. Phys. Lett.* **89**, 232114 (2006).
14. Conibeer, G. J., König, D., Green, M. A. & Guillemoles, J. F. Slowing of carrier cooling in hot carrier solar cells. *Thin Solid Films* **516**, 6948–6953 (2008).
15. Trinh, M. T. *et al.* Direct generation of multiple excitons in adjacent silicon nanocrystals revealed by induced absorption. *Nat. Photonics* **6**, 316–321 (2012).
16. Kim, S.-T., Kim, J.-H. & Lee, Y. H. PbS Quantum Dots: Carrier Multiplication in PbS Quantum Dots Anchored on a Au Tip using Conductive Atomic Force Microscopy (Adv. Mater. 17/2020). *Adv. Mater.* **32**, 2070130 (2020).

17. Sandeep, C. S. S. *et al.* High charge-carrier mobility enables exploitation of carrier multiplication in quantum-dot films. *Nat. Commun.* **4**, 2360 (2013).
18. Saeed, S. *et al.* Carrier multiplication in germanium nanocrystals. *Light Sci. Appl.* **4**, e251–e251 (2015).
19. de Weerd, C. *et al.* Efficient carrier multiplication in CsPbI₃ perovskite nanocrystals. *Nat. Commun.* **9**, 4199 (2018).
20. Gao, J., Fidler, A. F. & Klimov, V. I. Carrier multiplication detected through transient photocurrent in device-grade films of lead selenide quantum dots. *Nat. Commun.* **6**, 8185 (2015).
21. Hu, L. & Mandelis, A. Advanced characterization methods of carrier transport in quantum dot photovoltaic solar cells. *J. Appl. Phys.* **129**, 091101 (2021).
22. Carey, G. H., Levina, L., Comin, R., Voznyy, O. & Sargent, E. H. Record Charge Carrier Diffusion Length in Colloidal Quantum Dot Solids via Mutual Dot-To-Dot Surface Passivation. *Adv. Mater.* **27**, 3325–3330 (2015).
23. Rath, A. K. *et al.* Solution-processed inorganic bulk nano-heterojunctions and their application to solar cells. *Nat. Photonics* **6**, 529–534 (2012).
24. Johnston, K. W. *et al.* Efficient Schottky-quantum-dot photovoltaics: The roles of depletion, drift, and diffusion. *Appl. Phys. Lett.* **92**, 122111 (2008).
25. Sun, D. *et al.* Ultrafast hot-carrier-dominated photocurrent in graphene. *Nat. Nanotechnol.* **7**, 114–118 (2012).
26. Tielrooij, K. J. *et al.* Photoexcitation cascade and multiple hot-carrier generation in graphene. *Nat. Phys.* **9**, 248–252 (2013).
27. Winzer, T. & Malić, E. Impact of Auger processes on carrier dynamics in graphene. *Phys. Rev. B* **85**, 241404 (2012).
28. Zhou, S. Y. *et al.* First direct observation of Dirac fermions in graphite. *Nat. Phys.* **2**, 595–599 (2006).
29. Chen, Y., Li, Y., Zhao, Y., Zhou, H. & Zhu, H. Highly efficient hot electron harvesting from graphene before electron-hole thermalization. *Sci. Adv.* **5**, eaax9958 (2019).
30. Hot Carrier Extraction from Multilayer Graphene | Nano Letters. <https://pubs.acs.org/doi/abs/10.1021/acs.nanolett.6b02354>.
31. König, D. *et al.* Hot carrier solar cells: Principles, materials and design. *Phys. E Low-Dimens. Syst. Nanostructures* **42**, 2862–2866 (2010).
32. Kim, J. S. *et al.* Escalated Photocurrent with Excitation Energy in Dual-Gated MoTe₂. *Nano Lett.* **21**, 1976–1981 (2021).

33. Manser, J. S. & Kamat, P. V. Band filling with free charge carriers in organometal halide perovskites. *Nat. Photonics* **8**, 737–743 (2014).
34. Paul, K. K. *et al.* Strongly enhanced visible light photoelectrocatalytic hydrogen evolution reaction in an n-doped MoS₂/TiO₂ (B) heterojunction by selective decoration of platinum nanoparticles at the MoS₂ edge sites. *J. Mater. Chem. A* **6**, 22681–22696 (2018).
35. Paul, K. K., Mawlong, L. P. L. & Giri, P. K. Trion-Inhibited Strong Excitonic Emission and Broadband Giant Photoresponsivity from Chemical Vapor-Deposited Monolayer MoS₂ Grown in Situ on TiO₂ Nanostructure. *ACS Appl. Mater. Interfaces* **10**, 42812–42825 (2018).
36. Jung, E. H. *et al.* Efficient, stable and scalable perovskite solar cells using poly(3-hexylthiophene). *Nature* **567**, 511–515 (2019).
37. Tai, Q. *et al.* Efficient and stable perovskite solar cells prepared in ambient air irrespective of the humidity. *Nat. Commun.* **7**, 11105 (2016).
38. De Bastiani, M. *et al.* Efficient bifacial monolithic perovskite/silicon tandem solar cells via bandgap engineering. *Nat. Energy* **6**, 167–175 (2021).
39. Wong, J. *et al.* High Photovoltaic Quantum Efficiency in Ultrathin van der Waals Heterostructures. *ACS Nano* **11**, 7230–7240 (2017).
40. Fan, S., Vu, Q. A., Tran, M. D., Adhikari, S. & Lee, Y. H. Transfer assembly for two-dimensional van der Waals heterostructures. *2D Mater.* **7**, 022005 (2020).
41. Seo, S. *et al.* Amorphous TiO₂ Coatings Stabilize Perovskite Solar Cells. *ACS Energy Lett.* **6**, 3332–3341 (2021).
42. Kam, K. K. & Parkinson, B. A. Detailed photocurrent spectroscopy of the semiconducting group VI transition metal dichalcogenides. *J. Phys. Chem.* **86**, 463–467 (1982).

Data availability

The data that support the findings of this study are available from the corresponding author upon reasonable request.

Acknowledgements

This work was supported by the Institute for Basic Science of Korea (IBS-R011-D1) and Advanced Facility Center for Quantum Technology.

Author contributions: K.K.P. conceived the idea, and developed the project with the guidance of J.-H.K. and Y.H.L. K.K.P, J.-H.K. and Y.H.L. designed the experiments. K.K.P. fabricated all the devices with the help of A.M. K.K.P. performed all the optoelectronic and photovoltaic characterizations together with absorption, AFM and Raman measurements. J.W.K. contributed to the X-ray photoemission spectroscopy. K.K.P. and Y.H.L. interpreted the results, and wrote the manuscript. All authors discussed the results and commented on the manuscript. Y.H.L. supervised the entire project.

Competing interests

The authors declare no competing interests.

Additional information

Supplementary information The online version contains supplementary material available at

Figures and captions

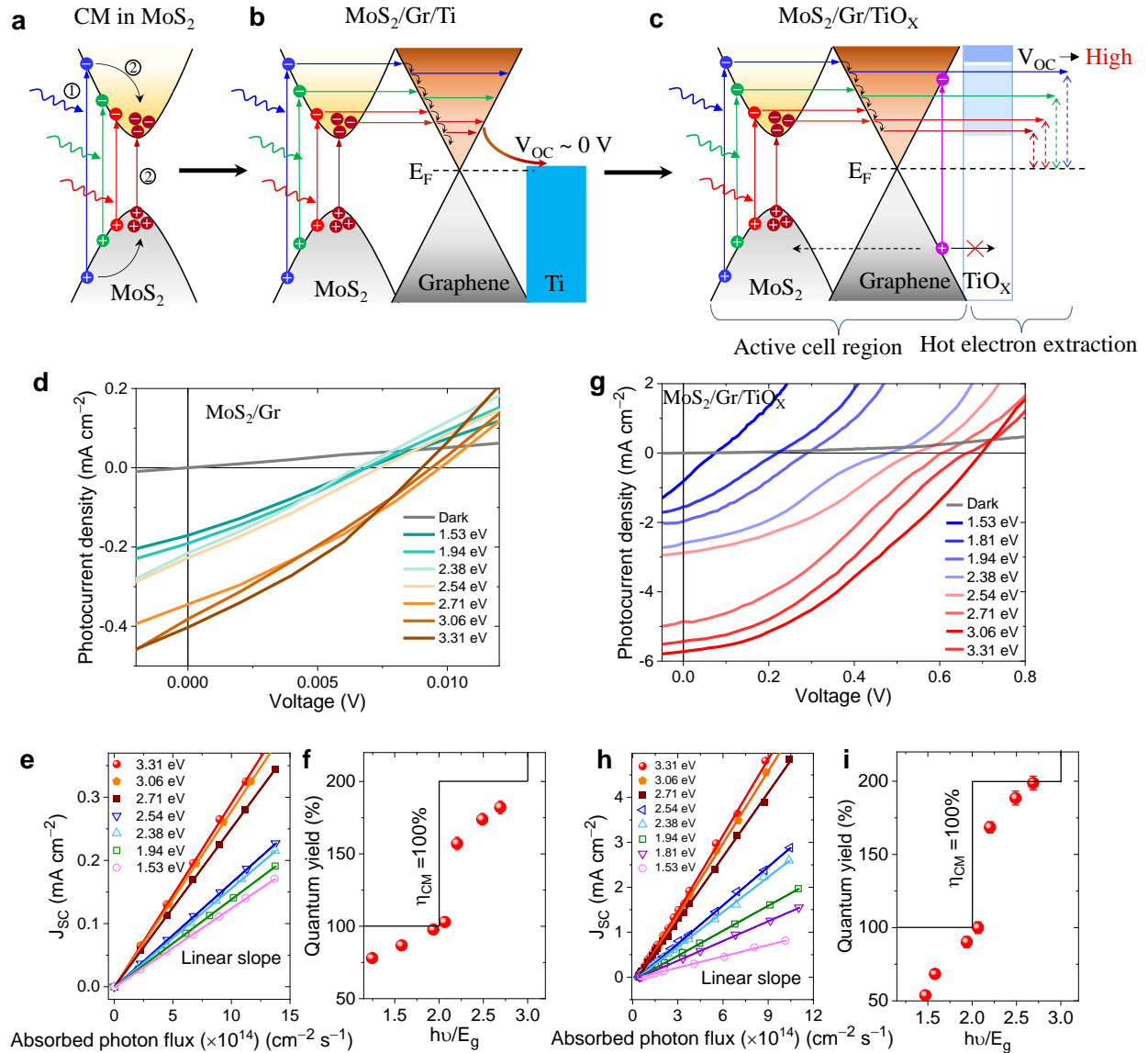


Fig. 1| Carrier multiplication and hot carrier-driven photovoltaics in MoS₂/Gr/TiO_x cell. a, CM in MoS₂ with an optical excitation above $2E_g$ (process 1) and generated by inverse Auger recombination (process 2). **b**, Photoexcited multicarriers in MoS₂ is transferred to Gr which generates abundant HCs due to phonon bottleneck effect, finally reaching Ti electrode. Negligible V_{OC} is detected between Gr and Ti electrode. **c**, TiO_x is deposited on Gr for broadband resonant tunneling layer to efficiently extract HCs to elevate V_{OC} . **d**, Current-voltage characteristics of MoS₂/Gr cell with the excitation of various energies at a fixed absorbed photon density ($\sim 1.4 \times 10^{15} \text{ cm}^{-2} \text{ s}^{-1}$). Maximum V_{OC} and J_{SC} are $\sim 10 \text{ mV}$ and 0.4 mA cm^{-2} at 3.31 eV , respectively. **e**, Linear plot of J_{SC} versus absorbed photon density upon optical excitations with various energies and **f**, CM conversion efficiency determined by the slope with respect to the bandgap of multilayer MoS₂

(1.23 eV)⁴². **g-i**, Similar characteristics of MoS₂/Gr/TiO_x cell. Similar CM conversion efficiency is achieved but with much higher V_{OC} (~0.7 eV) and improved J_{SC} (~5.7 mA cm⁻²).

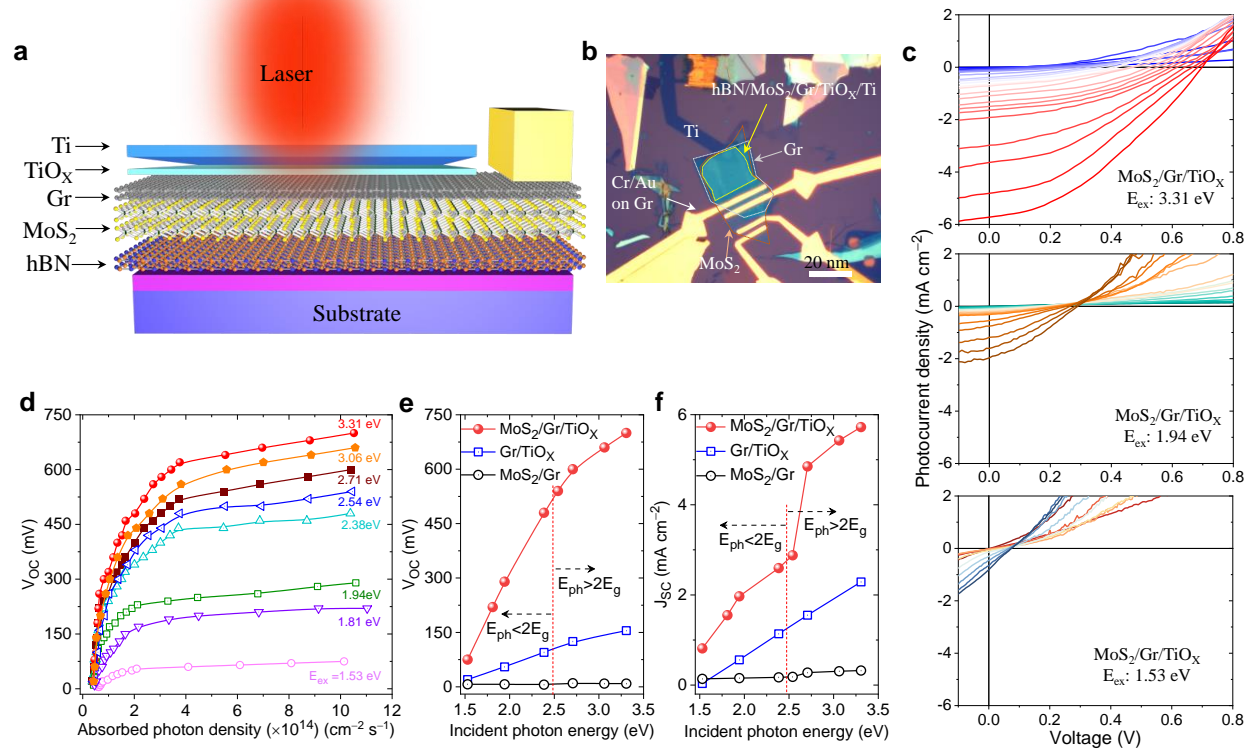


Fig. 2| Hot carrier-driven photovoltaic MoS₂/Gr/TiO_x cell. **a**, Schematic illustration of MoS₂/Gr/TiO_x cell with top Ti electrode (5 nm) fabricated on hBN substrate. **b**, Optical micrograph of the cell. **c**, Photocurrent density vs voltage with various photon densities (up to $\sim 1.1 \times 10^{15} \text{ cm}^{-2} \text{ s}^{-1}$) at different photon energies (3.31 eV, 1.94 eV and 1.53 eV). **d**, Open circuit voltage (V_{OC}) as a function of absorbed photon density for eight different energies. Variation of **e**, V_{OC} as well as **f**, J_{SC} with the incident photon energy at a fixed photon density ($1.1 \times 10^{15} \text{ cm}^{-2} \text{ s}^{-1}$) for different cells. MoS₂/Gr/TiO_x cell shows cascade photovoltaic characteristics (high V_{OC} and J_{SC}) compared to other cell architectures, confirming the coexistence of HC and CM.

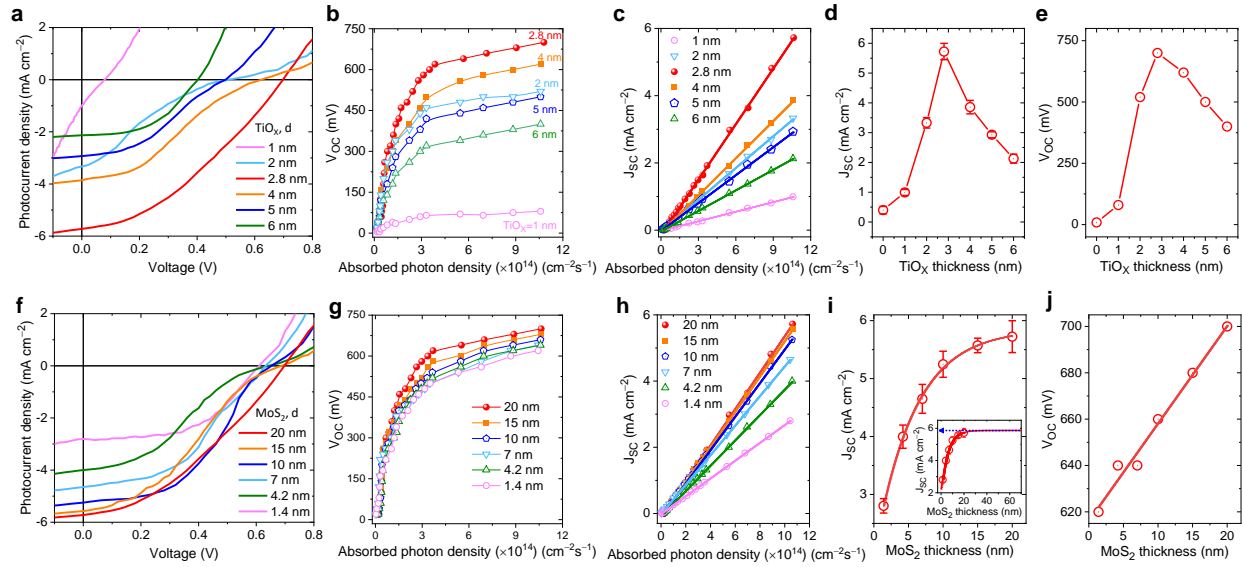


Fig. 3| Thickness dependence of BRT barrier and MoS₂ film on photovoltaics. **a**, Current-voltage characteristics of MoS₂/Gr/TiO_x/Ti cell with various BRT layer thicknesses (TiO_x: 1 ~ 6 nm) at 3.31 eV excitation. **b**, V_{OC} and **c**, J_{SC} as a function of absorbed photon density at 3.31 eV for different BRT layer thicknesses. Variation of **d**, J_{SC} and **e**, V_{OC} as a function of BRT layer thickness at 3.31 eV laser excitation and a fixed photon density ($\sim 1.1 \times 10^{15} \text{ cm}^{-2} \text{ s}^{-1}$). The optimum TiO_x layer thickness is determined as 2.8 nm with maximum V_{OC} = 0.7 V and J_{SC} = 5.7 mA cm⁻². **f**, Current-voltage characteristics of MoS₂/Gr/TiO_x/Ti cell with various MoS₂ film thicknesses (1.4 ~ 20 nm) at a fixed TiO_x layer thickness of 2.8 nm under 3.31 eV excitation. **g**, V_{OC} and **h**, J_{SC} as a function of absorbed photon density at 3.31 eV for different MoS₂ film thicknesses. **i**, J_{SC} increases linearly in thin MoS₂ layers and saturates at thick layers, while **j**, V_{OC} increases linearly. Extrapolation of the fitting shows that the maximum J_{SC} can reach as high as $\sim 5.87 \text{ mA cm}^{-2}$ (inset of **i**).

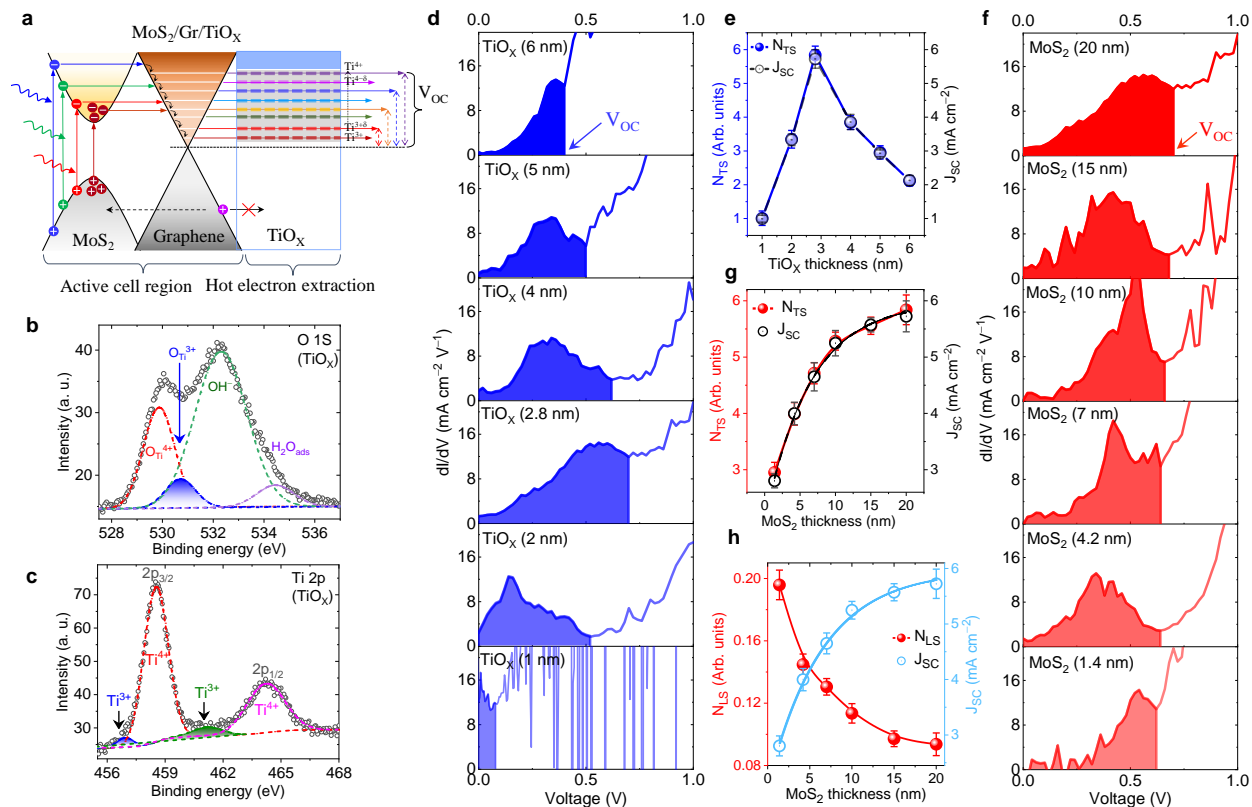


Fig. 4| Origin of broadband resonant tunneling. **a**, Cascade HC energies in Gr resonant with the various oxidation states in ultrathin BRT layer ($\text{Ti}^{3+\delta}$, $\delta = 0$ to 1) is the key for efficient HC extraction through broadband tunneling. **b**, O1s and **c**, Ti2p core level XPS spectra of TiO_x layer, fitted with Shirley baseline. Symbols represent the experimental data and the dashed lines correspond to the Gaussian fit. Fitted curves with filled area are associated with the various oxidation states of $\text{Ti}^{3+\delta}$, identifying the broadband resonant tunneling of HCs. Here, δ varies from 0 to 1. **d**, 1^{st} derivative of photocurrent with respect to the voltage (dI/dV) with various BRT layer thickness and **f**, MoS_2 film thickness. Each peak shows the corresponding resonant tunneling through the BRT layer. Number of available tunneling states, N_{TS} in the BRT layer with the variation of **e**, TiO_x and **g**, MoS_2 thickness. **h**, Number of leakage states, N_{LS} varying with MoS_2 thickness. Both the N_{TS} and N_{LS} are consistent with the corresponding J_{SC} values.

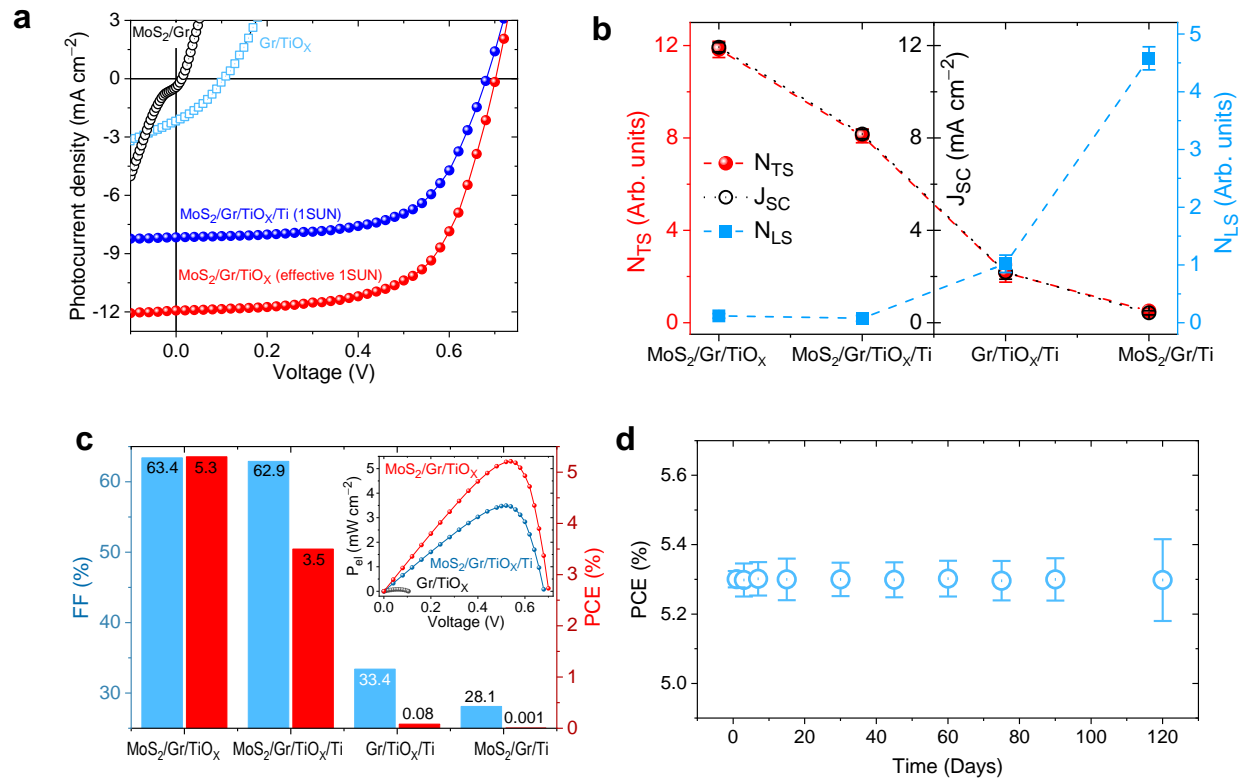
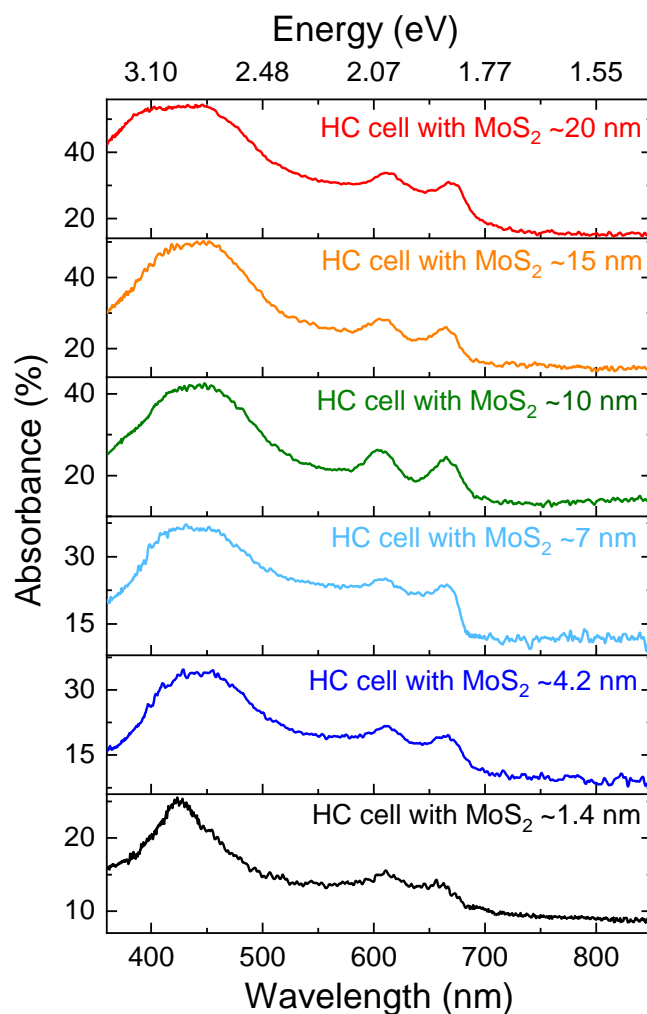
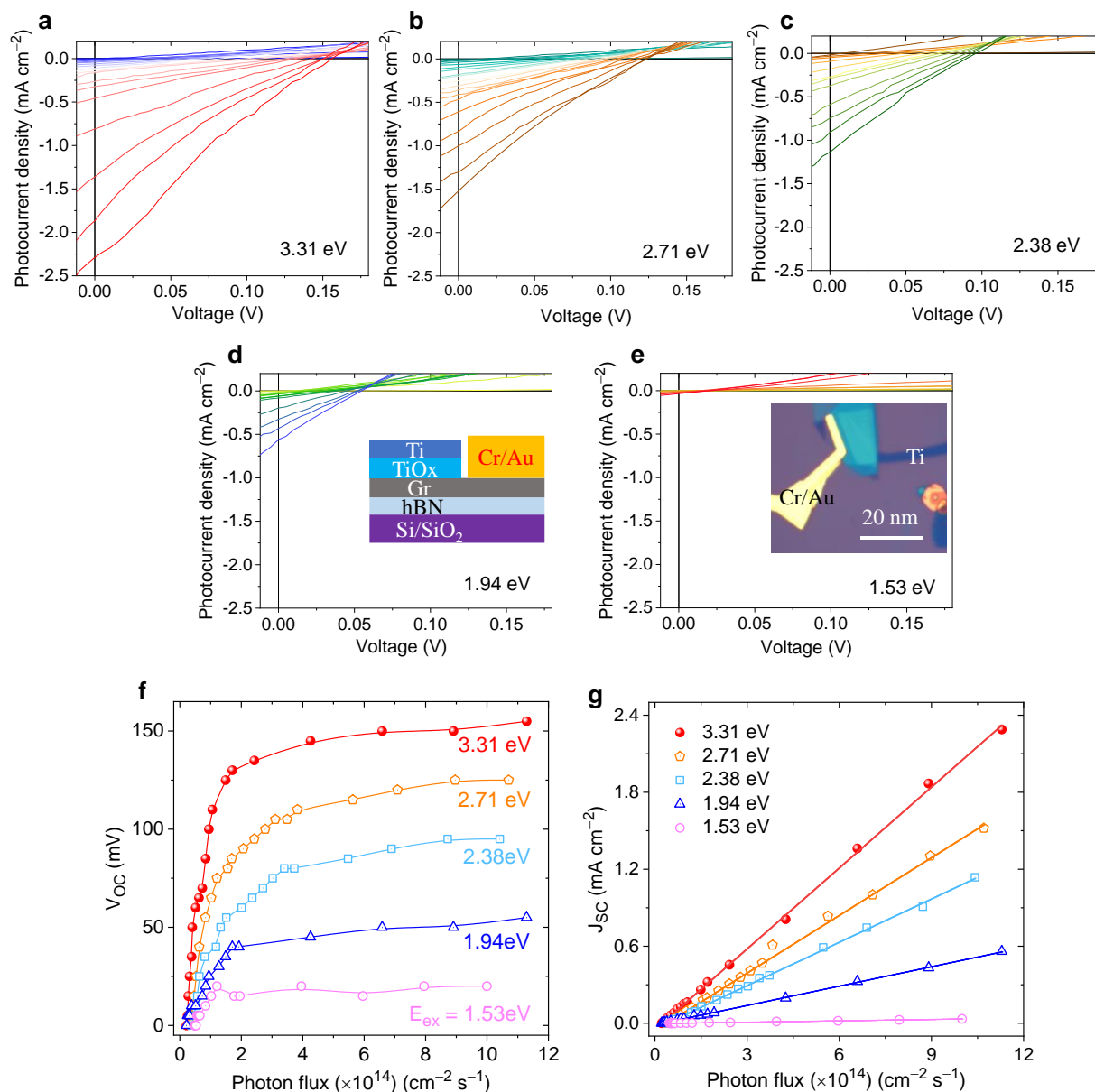


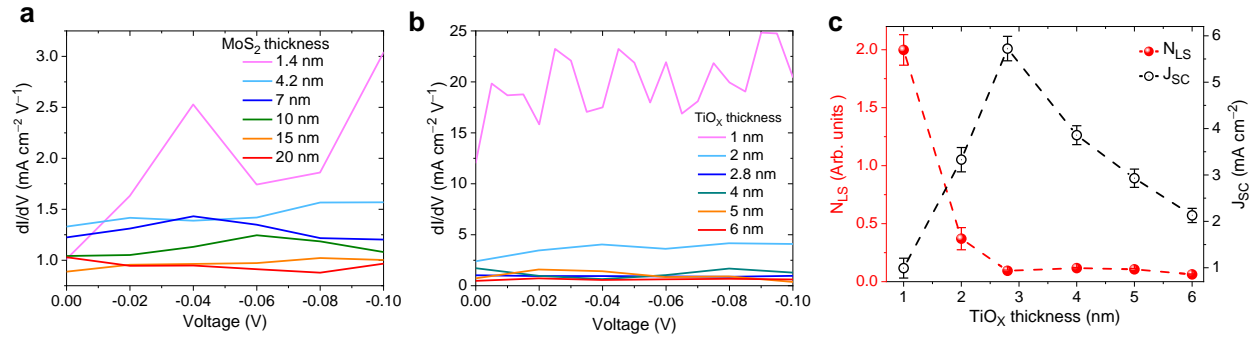
Fig. 5| Solar cell performance in 1-SUN of MoS₂/Gr/TiO_x cell. a, Measured photocurrent density vs. voltage for different cells (MoS₂/Gr/Ti, Gr/TiO_x/Ti, MoS₂/Gr/TiO_x/Ti and MoS₂/Gr/TiO_x). Transmittance of Ti layer (5 nm) is ~67%. 1-SUN of MoS₂/Gr/TiO_x is equivalent to 1.5-SUN of MoS₂/Gr/TiO_x/Ti. **b**, Number of available tunneling states (N_{TS}) at positive voltage and leakage states (N_{LS}) at negative voltage with corresponding J_{SC} values. **c**, Comparison of fill factor (FF), electric power density (P_{el}, inset), and power conversion efficiency (PCE) of various cells. MoS₂/Gr/TiO_x cell shows the maximum photovoltaic performance with PCE of 5.3%. **d**, Long-term operational stability of MoS₂/Gr/TiO_x cell under ambient conditions.



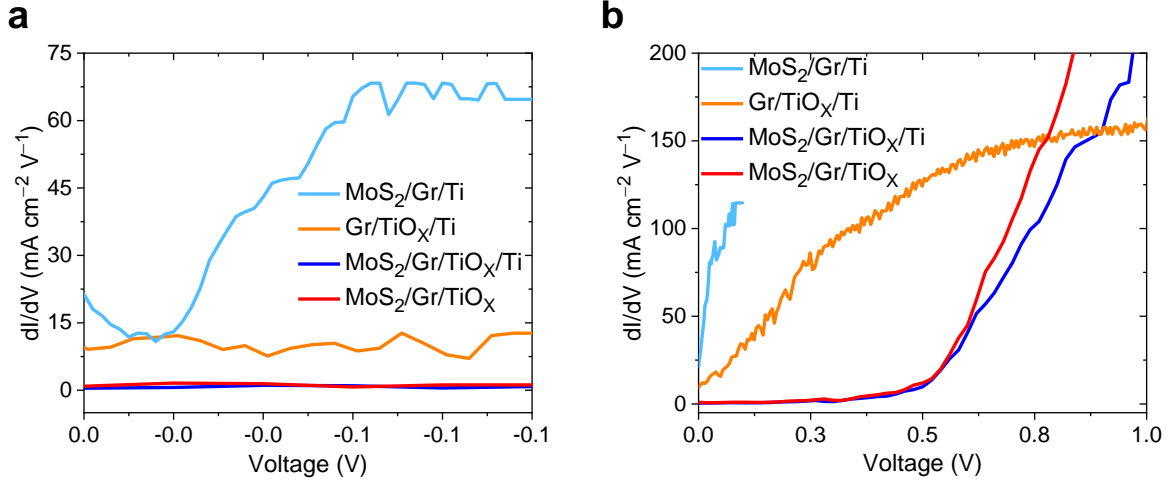
Extended Data Fig. 1| Optical absorbance of MoS₂/Gr/TiO_x/Ti cells. Optical absorbance of cells with various MoS₂ thicknesses. Reflectance and transmittance of the cells on quartz substrate were measured to calculate the absorbance.



Extended Data Fig. 2 | Hot carrier-driven photovoltaic Gr/TiO_x cell. **a-e**, Photocurrent density vs voltage with various photon densities (up to $\sim 1.2 \times 10^{15} \text{ cm}^{-2} \text{ s}^{-1}$) at different photon energies (3.31 eV, 2.71 eV, 2.38 eV, 1.94 eV and 1.53 eV). Schematic representation of Gr/TiO_x/Ti cell on hBN substrate is shown in inset of **d**, while the corresponding optical micrograph is depicted in inset of **e**. **f**, Open circuit voltage (V_{OC}) and **g**, short circuit current density (J_{SC}) as a function of photon density for five different energies, clearly revealing the HC extraction from Gr via resonant tunneling through BRT layer.



Extended Data Fig. 3 | Leakage states varying with MoS₂ and TiO_x thickness. 1st derivative of photocurrent with respect to the voltage (dI/dV) with various **a**, MoS₂ film and **b**, BRT layer thicknesses at negative voltage from 0 to -0.1 V. **c**, Number of leakage states (N_{LS}) in the BRT layer varying with TiO_x thicknesses. Leakage current dominates at low BRT layer thickness (1 nm) and rapidly falls with increasing TiO_x layer thickness over 2.8 nm.



Extended Data Fig. 4 | Leakage and tunneling states in various cells. dI/dV for **a**, leakage states at negative voltage from 0 to -0.1 V and **b**, tunneling states at positive voltage from 0 to 1 V.